The Passive Microwave Water Cycle Product

Kyle Hilburn
Remote Sensing Systems
http://www.remss.com

1. Introduction

The purpose of this technical report is to document the methodology we use for producing the Passive Microwave Water Cycle (PMWC) product. The PMWC product provides a full characterization of the atmospheric branch of the water cycle over the ocean, and it includes the parameters: water vapor, water vapor transport (speed and direction), water vapor transport divergence, evaporation, and precipitation. This product was developed for the NASA Energy and Water Cycle Study (NEWS) and is an extension of the work by Wentz et al. (2007). This report specifically describes the methodology used in producing the Version-1b PMWC product. The product has a spatial resolution of 0.25-degrees, a temporal resolution of one month, a time period from July 1987 through December 2006, and coverage over the global oceans observed by the SSM/I sensors (F08, F10, F11, F13, F14, and F15).

The PMWC product is available in a simple binary format. A "readme" text file describing the format is provided. We also provide FORTRAN, IDL, and MatLab read code and a text file to verify that the read code is working properly. The product is available on Remote Sensing Systems' (REMSS) public FTP server (ftp://ftp.remss.com/water_cycle/), a link to which can be found on the REMSS homepage (http://www.remss.com).

2. Construction of the Dataset

We will begin by describing the input data for the PMWC product: both the satellite data and the auxiliary data sets as well as our quality control measures and adjustments. We then discuss the details of our evaporation, precipitation, water vapor transport and divergence calculations. The evaporation and precipitation calculations are based on Wentz et al. (2007) with some important differences. The water vapor transport and divergence calculations have not been documented in detail before, and we will discuss the techniques we used along with some of the different methods we tried, notably feature tracking.

a. Input Data

There are many datasets needed to develop this product. The foundation dataset upon which all of this work is built is the REMSS Version-6 SSM/I geophysical retrievals. Earlier versions of SSM/I retrievals were sufficiently accurate for monitoring sea ice extent and water vapor because these two retrievals are relatively robust, requiring calibration accuracies of 0.2 K. Wind speed retrievals are more sensitive to calibration errors, however, and a climate-quality wind speed dataset requires calibration accuracies on the order of 0.05 K. Details about the Version-6 calibration method, including changes in the target factor approach and modeling of

F10 attitude anomalies, can be found in the Supporting Online Material (SOM) for Wentz et al. (2007). For the PMWC product, retrievals of wind speed, water vapor, and rain rate are used. The Version-6 wind speed retrievals have been validated using ocean buoys and have been compared with scatterometer wind retrievals (Wentz et al. 2007, SOM). The Version-6 rain rate retrievals from different sensors have been evaluated against each other for consistency and against other rain datasets (Hilburn and Wentz 2008a) and ocean buoys (Bowman et al. 2009).

The transport calculations require an estimate of wind direction, and for this we use the Version 1.1 Level 2.5 Cross-Calibrated Multi-Platform (CCMP) ocean surface wind product (Atlas et al. 2009). The CCMP wind product uses REMSS wind speeds and variationally assigns a wind direction. Where satellite data are available, the CCMP wind speeds are the same as REMSS wind speed retrievals. The PMWC product only uses CCMP directions where satellite data are available. We have performed extensive analysis of the CCMP product and find it to be a very high-quality dataset. We also use the National Centers for Environmental Prediction (NCEP) Global Data Assimilation System (GDAS) analysis of wind and humidity at different vertical heights in the development and testing of the feature tracking algorithm and for the surface to transport adjustment described further in Section 2.d.ii.

The evaporation calculations require an estimate of sea surface temperature (SST). Retrieval of SST for water warmer than 12°C is only possible using X-band channels (10.7 GHz). For colder water, C-band channels (6.9 GHz) are required. Thus, tropical SSTs are available starting in 1998 with TRMM and global SSTs are available starting in 2002 with AMSR-E. Since neither of these products is available before 1998, and in order to have consistent SST input, we use instead the NOAA/NCEP Reynolds optimal interpolation (OI) Version-2 SST (Reynolds et al. 2002). While of limited resolution, it is a widely used and quality-checked product available throughout the time period needed for construction of the PMWC dataset.

Evaporation is primarily driven by wind speed and SST, but the calculation also requires estimates of relative humidity and air-sea temperature difference. We obtain relative humidity from the International Comprehensive Ocean-Atmosphere Data Set (ICOADS) and air-sea temperature difference from the difference between the Hadley Center's Marine Air Temperatures (MAT) and Reynolds SST. Only nighttime MATs are used to avoid biases due to solar heating of ship decks. For both datasets, we average over the 19 years 1987-2006 and make 12 monthly climatological maps. The advantage of using a climatology is to prevent introducing spurious trends in relative humidity or air-sea temperature difference to our product that are hard to validate. We note that ICOADS relative humidity has no appreciable trends above the noise level, while the Hadley Center's MATs have a well known cooling trend (Christy et al. 2001). Full details are available in Wentz et al. (2007, SOM). Since Wentz et al (2007) were concerned with global average values and not spatial patterns, they did not spatially filter these climatological maps in any way. Since the PMWC product is at a higher resolution, and since spatial patterns are important, we applied the additional step of smoothing these climatological maps by fitting with spherical harmonics. Examination of spatial patterns of evaporation suggests that use of climatological information about relative humidity and air-sea temperature difference underestimates the atmospheric variability in meteorologically active regions (Pete Robertson, unpublished work).

The rain to snow adjustment is required as described in Section 2.c. The adjustment makes use of the Global Precipitation Climatology Project (GPCP) Version 2 rain rates (Adler et al. 2003) and is a function of latitude and month, derived from data averaged over 1988-2005.

We apply a number of quality control procedures: 1) F15 retrievals after 14 August 2006 are excluded because of degradation due to the RADCAL beacon. The beacon yields data too unreliable for climate study (Hilburn and Wentz 2008b, Hilburn 2009). 2) Area ice flagging has been performed by excluding pixels (pixel is a 0.25° box) that have ice within a 5x5 area. 3) Pixels containing rain have been excluded from the evaporation and transport calculations. We have not performed area rain flagging, which is typical for climate applications. This choice was made to obtain more data near raining areas. 4) A classic 3x3 smoothing filter with binomial coefficients (Gonzalez and Woods 2002) has been applied to reduce high-frequency noise. This is particularly beneficial for the transport and divergence, which tend to be noisy. 5) Pixels containing an insufficient number of observations to produce a monthly average are classified as land or ice depending upon whether SSM/I identified land or ice in that pixel during the month.

PMWC versions after Version-1 apply a post-hoc wind correction described in Wentz et al. (2007, SOM). The correction was originally omitted purposely because of its small nature. However, collaboration with Pete Robertson showed that this small correction makes an important contribution to the variability of the global ocean average evaporation time series. The post-hoc correction is a table of 20 numbers that correspond to SSM/I minus buoy wind speed for each year. This small empirical adjustment brings the SSM/I winds in agreement with the buoy winds. The magnitude of the annual adjustments is about 0.1 m/s or less, and they have no net effect on the overall trend. That is to say, the 20 numbers in the correction table have been de-trended. Figure S1 in Wentz et al. (2007) shows the adjustment. Figure 1 shows PMWC evaporation time series both before and after the wind correction. As you can see, the correction has no effect on the trend (1.26%/decade), but nearly doubles the evaporation anomaly from El Nino in 1998.

b. Calculating Evaporation

Evaporation, *E*, is calculated using the bulk aerodynamic method:

$$E = 3.6\rho_{air} C_E u_* \left(q_s - q_a\right) \tag{1}$$

where ρ_{air} is the density of air, C_E is the drag coefficient, u_* is the friction velocity, q_s is the specific humidity at the sea surface, q_a is the specific humidity at height *z*, and the factor of 3.6 gives units of mm/hr. The calculations are performed at a height of z = 15 m, the height of the air-sea temperature difference and relative humidity climatologies. Specific humidity and air density are calculated using the Goff-Gratch formulation (Cruz Pol and Ruf 1998). At the surface, q_s is calculated using Reynolds SST and assuming saturation (relative humidity of 100%). A factor of 0.981 is applied to account for the effects of salinity. At the reference height, q_a is calculated using Reynolds SST, our climatological air-sea temperature difference, and the climatological relative humidity. We assume that the atmospheric pressure is 1013.246 mb. The friction velocity is calculated based on Large and Pond (1982):

$$u_* = \left(0.0027w + 0.000142w^2 + 0.0000764w^3\right)^{1/2} \tag{2}$$

where w is the 10-m wind speed measured by SSM/I. The drag coefficient is given by Monin-Obukhov similarity theory, which was implemented following Collins et al. (2004). In this formulation the drag coefficient is a function of: reference height, SST, air temperature at the reference height, specific humidity at the surface and the reference height, and u_*.

c. Calculating Precipitation

Precipitation, P, is calculated using the Version-6 SSM/I rain rate retrievals. The Version-6 rain retrievals (Hilburn and Wentz 2008a) are far superior to the Version-5 retrievals (Wentz and Spencer 1998). The Version-5 rain retrievals were about 60% too high in the tropics due to unrealistic assumptions about the freezing level. These assumptions have been corrected. Version-5 rain retrievals also had intersensor biases as large as 30%. The intersensor biases were removed after making three changes: 1) a consistent optimal interpolation technique is now used for all sensors to resample antenna temperatures to common spatial resolutions, 2) the beamfilling correction now models the effects of radiometer saturation for the 19 and 37 GHz channels, and 3) the beamfilling correction now explicitly models the effects of radiometer footprint size. The changes to the beamfilling correction were determined by simulating SSM/I data with higher resolution AMSR-E data. That is to say, the changes made to the beamfilling algorithm have a firm physical basis, and there was no "tuning". Full details about the Version-6 rain rates can be found in Hilburn and Wentz (2008a).

The Version-6 rain rates from SSM/I now have small intersensor biases on the order of 3%. While the diurnal cycle of rain over the ocean is smaller than over land, it is not negligible, and failure to account for the different satellite local crossing times yields inconsistencies on the order of 1-3% (Hilburn and Wentz 2008a). Another 1-2% of the discrepancy has yet to be identified, although likely sources include nonlinearity in the calibration equation or multiplicative errors arising from small errors in the spillover or hot load specification. For use in climate analysis, the rain rates are adjusted by a few percent with a static, global value for each platform. A table of the values can be found in Hilburn and Wentz (2008a).

Passive microwave measurements below 37 GHz are not very sensitive to frozen precipitation (i.e., snow), yet proper hydrological balance requires that we account for snow. Wentz et al. (2007) found that without adjusting for snow, the Version-6 rain rates were about 18% too low to meet hydrological balance. They also found that GPCP rain rates balanced evaporation almost perfectly, and that the source of the SSM/I rain rate discrepancy was in high latitudes. The discrepancy was found to occur in the wintertime in regions identified by Petty's (1995) ship observations as snowing regions. We take this to imply that a latitudinal and seasonally dependent snow correction is necessary. The snow correction that we use is shown in Figure 2. The adjustments reach as large as a factor of 3 in the winter hemispheres poleward of 30° latitude. The correction has been smoothed by fitting harmonics and is set to 1 equatorward of 30° latitude. The net effect of the snow adjustment is to increase the global-ocean-average precipitation by 18%.

d. Calculating Water Vapor Transport and Divergence

The original intention of our work was to develop an independent estimate of precipitation using an estimate of water vapor transport ($\vec{\mathbf{Q}}$) from satellite data and hydrological balance on monthly time scales (Peixoto and Oort 1992) given by

$$\nabla \bullet \vec{\mathbf{Q}} = E - P \tag{3}$$

where ($\nabla \bullet \vec{\mathbf{Q}}$) is the water vapor transport divergence. To estimate water vapor transport, we planned to use feature tracking on successive water vapor images. Unfortunately, despite our best efforts, we were unable to obtain good results using this method. The first part of this section will describe our work on the feature tracking algorithm and discuss why feature tracking doesn't work well enough. The problem lies not so much in estimating the transport, but in the divergence fields calculated from the transport. Feature tracking can give the right large-scale pattern, but the divergence comes from the small-scale information in the transport field. The second part of this section then describes how we used satellite derived surface winds to obtain transport and divergence estimates. Unfortunately, even though using surface winds gave much improved results over feature tracking, the estimates of divergence still had regional errors that were as large as the signal itself. We decided then to sacrifice independence in order to obtain good quality transport fields. The technique used in the PMWC product uses the surface winds and water vapor to obtain a first guess transport field, and then adjusts the vectors until the divergence matches *E-P*. The third part of this section will describe this adjustment technique.

i. Feature Tracking Algorithm

The basic idea behind feature tracking (Jedlovec et al. 2000) is to start with an image at time *t* and select a sub-image about a point (*i, j*) that is referred to as a "template". Then take an image at time *t+dt* and compare sub-images in the neighborhood of (*i, j*) to the template. Comparing a number of sub-images, one then either minimizes a distance (difference) measure or maximizes a correlation measure. The result is the "match", a sub-image at point (*i+di, j+dj*). The velocity is then found to be (*di, dj*)/*dt* scaled by the factors appropriate to the map grid.

Feature tracking has a number of limitations. First, it has limited precision. Say that we have 0.25-degree water vapor maps every 6 hours. This means the precision of the calculated transport speed is approximately 25 km / 6 hours / (3.6 km/hr / m/s) $\approx$ 1 m/s. Averaging to monthly time scales will reduce this, but it still significantly contributes to errors in the divergence. Even a 10% error in the transport components can yield a 100% error in the divergence (Holton 2004). The second problem is that water vapor is not conserved, even on 6-hour time scales. This is especially a problem in the tropics where there is heavy precipitation. A third problem is the so-called aperture problem: whenever you are estimating motion using successive images, you are unable to resolve motion along the image gradients. Again, we found this problem to be greatest in the tropics where features move more slowly than in the middle latitudes. A fourth problem is that since we only have data over the ocean, feature tracking has errors when features disappear over land or appear from the land to the ocean. This creates near coast artifacts and is the biggest problem in the northern hemisphere where there is the most land. A fifth problem is that feature tracking is a computationally expensive algorithm and the computer code can be very slow if not done right. These limitations were known at the beginning of the project, but their impact on transport estimates was not fully appreciated.

We tested our feature tracking algorithm by simulating water vapor maps with NCEP GDAS data. Vertically integrating GDAS humidity fields provided maps of water vapor. We applied feature tracking to these simulated water vapor maps to obtain water vapor transport. These transports were then compared with "true" water vapor transport obtained by vertically integrating GDAS humidity and wind fields. Thus, accurate estimates of error in the transport and divergence fields were possible without relying on any assumptions about water cycle closure.

In implementing the feature tracking algorithm, there are a number of parameters that must be chosen that have an effect on the overall accuracy of the technique. First, one must decide on a template size. If the template is too small, there is not enough image structure in it and the random error is larger. If the template is too large, then the resulting vector will not be representative of the actual motion. We found, by trial-and-error, that a template diameter of 11° worked best. Feature tracking also requires smoothing or filtering of some kind. We found that a 5° wide boxcar worked best compared to smaller or larger sizes. For the choice of match criterion, we found that the maximum correlation was superior. Feature tracking algorithms also generally use a number of quality control measures. Since we had an accurate estimate of the "truth" we were able to objectively test various measures. We found that comparing different match criterion did not provide additional information and we found that using image gradients and other estimates of texture to quality control the vectors did not help. The one quality-control measure that did help somewhat was comparing estimates obtained from tracking forwards in time versus backwards in time.

Using the parameter choices described above, we found that feature tracking on 6-hourly time scales provided transport estimates with instantaneous errors around 4.3 m/s speed RMS and 55° directional RMS. Averaging over a month reduced the errors to 2.2 m/s speed RMS and 46° directional RMS. These values are from January 2003, which is a typical example. While monthly average transport maps (Fig. 3) show an encouraging amount of correct detail, the divergence maps (Fig. 3) calculated from the transport show structures that are completely wrong. If the water budget is properly closed, maps of water vapor transport divergence are the same as maps of evaporation minus precipitation (Eqn. 3). Since evaporation has a smoother spatial pattern than precipitation, and since precipitation is generally larger than evaporation where there is precipitation; maps of water vapor transport divergence should look similar to maps of precipitation (with the color scale reversed). The water vapor transport divergence maps obtained by feature tracking look nothing like precipitation; but are filled with seemingly random noisy structures, coastal artifacts, and have no indication of the ITCZ.

We have also tried initializing the feature tracking search using the satellite derived wind vectors from CCMP. While this did improve the water vapor transport somewhat, the divergence was not improved. We mention here that we also tried more sophisticated optical flow techniques including the Horn and Schunck (1981) and Lucas and Kanade (1981) techniques. These actually performed a little bit worse than feature tracking, which is due to the fact that these techniques are more sensitive to the non-conservation of water vapor.

ii. Use of Surface Wind Information

Our work with the wind speed initialization for feature tracking showed us that the surface winds contain information about water vapor transport. Transport speeds from feature tracking have a correlation of R^2=0.55 with the true simulated transports, while surface wind speeds (with no adjustment) have a correlation of R^2=0.64. Clearly, there is useful information in the surface wind speeds. With an adjustment for the change in wind with height and the humidity profile, the surface winds and water vapor can be used to calculate transport. Since passive microwave can only accurately measure wind speed, we make use of the CCMP product, which variationally assigns a wind direction to REMSS V6 SSM/I wind speeds.

Figure 4 shows a schematic of the water vapor transport adjustment needed when using surface winds. Since specific humidity decreases exponentially with height, most of the columnar water vapor is found in the boundary layer – this is why the surface wind vector contains so much vapor transport information. Using the NCEP wind and humidity profiles, and comparing the vertically integrated water vapor transport velocities with the NCEP surface winds, we find that the global adjustment (averaged over 2003) is an increase in the surface wind speed by a factor of 1.4 and a rotation in the direction by 7° anticyclonically (a positive or clockwise adjustment in the northern hemisphere and a negative or counterclockwise adjustment in the southern hemisphere). Figure 5 shows the adjustment as a function of latitude, and for PMWC we use the following fits:

$$s = 1 + 0.75\left(1 - \cos\left(2 \bullet \phi\right)\right)/2 \tag{4a}$$

$$d = 18 \bullet \left(\phi / 90\right) \tag{4b}$$

where s is the speed scaling, d is the direction rotation, and ϕ is latitude in degrees. We have also tried more complicated adjustments that are functions of longitude, latitude, and month, but we found this produced odd artifacts (particularly in the eastern Pacific) due to mismatch between the satellite and model hydrological cycles. Note that any sort of climatological speed and direction adjustment is inherently large-scale (i.e., smooth). This means that while the adjustment improves the transport, it makes very little impact on the divergence, which is given by small-scale information in the transport field.

The results using CCMP wind vectors, SSM/I water vapor, and the surface to transport vector adjustment (Eqns. 4a and 4b) are shown in Figures 6, 7, 8, and 9. These figures compare results with and without the divergence adjustment that will be described later in Section 2.d.iii. Figure 6 (left) shows that there is a 100% global bias in the water vapor transport compared to *E-P*. Figure 7 (left) shows that water vapor transport divergence has the same basic pattern as *E-P*, but that the magnitude is more than twice what it should be. Figure 8 (left) shows that the errors in divergence are, for the most part, unbiased outside of extreme values. This suggests that the divergence errors are due to random errors in the transport components. What this means for hydrological balance is well summarized in Figure 9. The figure shows that evaporation minus water vapor transport divergence, which should equal precipitation, can be different by more than 100%. The divergence gives a much stronger ITCZ and SPCZ with no rain right on the equator. It is interesting to note that the evaporation minus divergence matches the rain rate more closely than the precipitation curve that has had the snow adjustment applied. Unfortunately, given the uncertainties in the divergence, it is impossible to draw any conclusions from this.

One factor that can explain some of the discrepancy in the transport divergence is the lack of transport information in and around raining areas. Where there is rain, we have no satellite wind information. Figure 10 shows the results from using the Atlas et al. (2009) Level 3 CCMP winds in raining areas to calculate transport. Note that while this does not fully close the water budget, it does make it dramatically better.

Where there is rain, and no satellite wind retrievals, Level 3 CCMP blends in ECMWF winds. These ECMWF data produce a large trend in CCMP – three times larger than the trend reported in Wentz et al. (2007). When CCMP data are rain flagged, the trend is the same as Wentz et al. (2007). While such a large trend seems unrealistic, if storms are becoming larger or stronger with global warming, then it is possible that the winds may have larger trends than a rain flagged analysis indicates.

iii. Divergence Adjustment Algorithm

In order to obtain realistic estimates of divergence, the transport vectors must be adjusted until the divergence equals *E-P*. This technique was based on previous work by Hilburn et al. (2003). Applying Helmholtz Theorem (Holton 2004), we can write:

$$E - P = -\nabla^2 \Phi_1 \tag{5a}$$

$$\nabla \bullet \vec{\mathbf{Q}} = -\nabla^2 \Phi_2 \tag{5b}$$

where Φ_1 and Φ_2 are potential functions. We solve each equation using successive over-relaxation (Press et al. 1992). Then if $\vec{\mathbf{Q}}$ is the transport without adjustment, and if $\vec{\mathbf{Q}}_A$ is the adjusted transport, then

$$\vec{\mathbf{Q}}_A = \vec{\mathbf{Q}} - \nabla \Phi_2 + \nabla \Phi_1 \tag{6}$$

For the PMWC product we used Dirichlet boundary conditions, and to be consistent with Wentz et al. (2007) we used their values of *E-P* = (527-806)/8766 mm/hr over land and *E-P* = (28-169)/8766 mm/hr over ice. Land and ice were determined as described in Section 1.a. Also, before solving (5a) and (5b), any residual global imbalance in E-P or $\nabla \bullet \vec{\mathbf{Q}}$ must be subtracted. Figure 11 shows how the vectors change with the adjustment. The adjustment serves mostly to rotate the vectors with a median rotation of 12°. Revisiting Figs. 6-9, we see that the divergence adjustment is crucial to obtaining realistic divergence values because without the adjustment, errors in the divergence are dominated by random errors in the transport.

This technique is similar to Sohn et al. (2004), who estimated transport by directly inverting (3) with different inputs for *E* and *P*. However, they were only able to obtain the nonrotational (i.e., divergent) component of the wind. Since we use the adjusted surface winds and columnar water vapor as a first guess, we are able to obtain the full transport vector (nonrotational + nondivergent) parts.

3. Characterization of the Dataset

Climate signals in SSM/I derived evaporation, precipitation, and water vapor have been described in Wentz et al. (2007), Hilburn and Wentz (2008a), and Wentz and Schabel (2000).

Since little attention has been paid to water vapor transport and divergence, this section will focus on characterizing these two parameters. We compare PMWC transport and divergence against Tim Liu's transport product, which was also developed for the NEWS project. The Liu transport product provides data over the tropical ocean -40° to 40° latitude at 0.5° spatial resolution. The product is available at daily temporal resolution and covers the period August 1999 through 2007. The details of the Liu methodology have changed slightly over time, but the basic idea is to use wind vectors from QuikSCAT, adjust them to transport vectors using some method, and then combine these vectors with water vapor from TMI and/or SSM/I. Liu and Tang (2005) used neural nets to adjust the surface wind vector to a transport vector. Xie et al. (2008) used support vector regression with the surface wind and also the 850 mb wind from MISR and geostationary cloud drift winds.

Figure 12 shows that, on the large scale, PMWC and Liu transports agree, with the most disagreement found at higher latitudes. This is confirmed by inspecting two-dimensional PDFs (Fig. 13). Despite the large-scale similarities in transport, there is disagreement in transport divergence (Fig. 14). The Liu product has much stronger convergence in the ITCZ. Joint PDFs (Fig. 15) show that the Liu product obtains much larger divergence and convergence values than PMWC. The zonal average precipitation implied by hydrological balance (that is, $P = E - \nabla \bullet \vec{\mathbf{Q}}$) for Liu (Fig. 16) is reminiscent of the unadjusted PMWC product (Fig. 9).

It is clear that what matters for the water cycle is the divergent component of the transport. Any analysis of a transport product should include analysis of the divergence of the transport. This is because while a particular transport product might compare favorably with validation data, a traditional validation only provides information of large-scale characteristics, whereas the divergence comes from the small-scale information in the transport field. On the other hand, only relying on the water cycle closure to evaluate a transport product is also misleading since, for a given divergence field, there is not one unique transport field, but an infinite number of transport fields that will satisfy the divergence.

Due to the fact that random errors in transport are dominated by the errors in divergence, examination of differences between divergence fields and *E-P* fields provides only limited physical insight. This is similar to the "vertical velocity problem" in meteorology, where it is well known that using the "kinematic method" of estimating vertical velocity from the horizontal divergence requires the use of additional constraints to reduce the random errors (O'Brien 1970). The most straightforward solution is to force the closure, which is what we have done for the PMWC product. Another approach is to use some sort of adaptive "smoothing" on the transports, which is what Liu had done by introducing 850 mb wind information.

Examining residual differences between global-averaged evaporation and precipitation (e.g. Wentz et al. 2007) proved fruitful because the analysis provided information about systematic errors. Examining maps of the residual difference between transport divergence and *E-P* has not proven as fruitful because random errors in the transport are dominated the divergence errors. One way to reduce the random errors would be to average over large areas, for example "ocean" and "land". In practice, this is made difficult by: different definitions of "ocean" and "land", different capabilities of how close to land different satellite sensors can measure, and a large

amount of heavy rain that falls in coastal areas and over small islands (Tajdarul Hassan Syed, unpublished work).

4. Conclusions and Future Work

This technical report has described in full detail how we calculated evaporation, precipitation, water vapor, transport, and divergence on monthly time scales from the REMSS Version-6 SSM/I dataset. The techniques discussed apply specifically to the Version-1b PMWC dataset produced for the NASA Energy and Water Cycle Study (NEWS) and are available at www.remss.com. We did not make use of TMI and AMSR-E retrievals in these products, as those instruments have slightly different climate signals than the SSM/I. This is not surprising because they have not been intercalibrated to the same level of accuracy on climate time scales as the SSM/I sensors. The climate signals in TMI are much closer to SSM/I than AMSR-E, because the calibration techniques used for TMI are more similar to SSM/I than AMSR-E. In the future, we hope to analyze these differences in detail and bring their calibration in line with SSM/I so that they can be included in PMWC. There is also more calibration work needed for SSM/I, particularly on F14 near the end of its life (after 2006 to 2008). The thermal environment of F14 was changing dramatically in this time period, and the Version-6 calibration (developed in early 2006) needs updating to properly handle all of the changes. We plan to add SSMIS to the PMWC product, and work is already underway to intercalibrate it with the SSM/I record. SSMIS should be extremely helpful for 2006 onward when the number of SSM/I decreases. Finally, we also hope to add WindSat to the dataset, which should not only provide better sampling, but also provides wind vectors which will be interesting to compare with CCMP vectors.

Acknowledgements

This work has been supported by the NASA Energy and Water Cycle Study (NEWS) under Contract NNG05OAR4311111. SSM/I data are produced by Remote Sensing Systems and sponsored by the NASA Earth Science MEaSUREs DISCOVER Project. Data are available at www.remss.com.

References

Adler, R. F., G. J. Huffman, A. T. C. Chang, R. Ferraro, P. Xie, J. E. Janowiak, B. Rudolf, U. Schneider, S. Curtis, D. T. Bolvin, A. Gruber, J. Susskind, P. A. Arkin and E. Nelkin, (2003) The version-2 Global Precipitation Climatology Project (GPCP) monthly precipitation analysis (1979-Present), *Journal of Hydrometeorology, 4*, 1147-1167.

Atlas, R. M., R. N. Hoffman, J. Ardizzone, S. M. Leidner and J. C. Jusem, Development of a new cross-calibrated, multi-platform (CCMP) ocean surface wind product, paper presented at AMS 13th Conference on Integrated Observing and Assimilation Systems for Atmosphere, Oceans, and Land Surface (IOAS-AOLS), Phoenix, AZ, 2009.

Bowman, K. P., C. R. Homeyer, and D. G. Stone, 2009. A comparison of oceanic precipitation estimates in the tropics and subtropics, *Journal of Applied Meteorology and Climatology, 48*, 1335-1344.

Christy, J. R., D. E. Parker, S. J. Brown, I. Macadam, M. Stendel and W. B. Norris, (2001) Differential trends in tropical sea surface and atmospheric temperatures since 1979, *Geophysical Research Letters, 28(1)*, 183-186.

Collins, W. D., P. J. Rasch, B. A. Boville, J. J. Hack, J. R. McCaa, D. L. Williamson, J. T. Kiehl, B. P. Briegleb, C. M. Bitz, S. J. Lin, M. Zhang and Y. Dai, (2004), Description of the NCAR Community Atmosphere Model (CAM 3.0), vol. TN-464+STR, edited by NCAR.

Cruz Pol, S. L. and C. S. Ruf, (1998) Improved 20- to 32- GHz atmospheric absorption model, *Radio Science, 33*(5), 1319-1333.

Gonzalez, R. C. and R. E. Woods, Digital Image Processing, Prentice Hall, Upper Addle River, New Jersey, 2002.

Hilburn, K. A., M. A. Bourassa and J. J. O'Brien, (2003) Development of scatterometer-derived surface pressures for the Southern Ocean, *Journal of Geophysical Research, 108*(C7), 3244, doi:10.1029/2003JC001772.

Hilburn, K. A. and F. J. Wentz, (2008a) Intercalibrated passive microwave rain products from the Unified Microwave Ocean Retrieval Algorithm (UMORA), *Journal of Applied Meteorology and Climatology, 47*, 778-794.

Hilburn, K. A. and F. J. Wentz, (2008b) Mitigating the impact of RADCAL beacon contamination on F15 SSM/I ocean retrievals, *Geophysical Research Letters, 35*, L18806, doi:10.1029/2008GL034914.

Hilburn, K. A., (2009), Including temperature effects in the F15 RADCAL correction, report number 051209, Remote Sensing Systems, 11 pp.

Holton, J. R., An Introduction to Dynamic Meteorology, Elsevier Academic Press, San Diego, CA, 2004.

Horn, B. K. P. and B. G. Schunck, (1981) Determining optical flow, *Artificial Intelligence, 17*, 185-203.

Jedlovec, G. J., J. A. Lerner and R. J. Atkinson, (2000) A satellite-derived upper-tropospheric water vapor transport index for climate studies, *Journal of Applied Meteorology, 39*, 15-41.

Large W. G., and S. Pond, (1982) Sensible and latent heat flux measurements over the ocean. *Journal of Physical Oceanography*, 12, 464–482.

Liu, W. T. and W. Tang, (2005) Estimating moisture transport over oceans using space-based observations, *Journal of Geophysical Research, 110*, D10101, doi:10.1029/2004JD005300.

Lucas, B. and Kanade, T. 1981. An iterative image registration technique with an application to stereo vision, in Proc. Seventh International Joint Conference on Artificial Intelligence, Vancouver, Canada, pp. 674–679.

O'Brien, J. J., (1970) Alternative solutions to the classical vertical velocity problem, *Journal of Applied Meteorology*, 9, 197-203.

Peixoto, J. P. and A. H. Oort, Physics of Climate, American Institute of Physics, Springer-Verlag, New York, NY, 1992.

Petty, G. W., (1995) Frequencies and characteristics of global oceanic precipitation from shipboard present-weather reports, *Bulletin of the American Meteorological Society, 76*(9), 1593-1616.

Press, W. H., S. A. Teukolsky, W. T. Vetterling and B. P. Flannery, Numerical Recipes in Fortran 77, Cambridge University Press, Cambridge, 1992.

Reynolds, R. W., N. A. Rayner, T. M. Smith, D. C. Stokes and W. Wang, (2002) An improved in situ and satellite SST analysis for climate, *Journal of Climate, 15* , 1609-1625.

Sohn, B.-J., E. A. Smith, F. R. Robertson and S.-C. Park, (2004) Derived over-ocean water vapor transports from satellite-retrieved E - P datasets, *Journal of Climate, 17*(6), 1352-1365.

Wentz, F. J. and R. W. Spencer, (1998) SSM/I rain retrievals within a unified all-weather ocean algorithm, *Journal of the Atmospheric Sciences, 55*(9), 1613-1627.

Wentz, F. J. and M. C. Schabel, (2000) Precise climate monitoring using complementary satellite data sets, *Nature, 403*(6768), 414-416.

Wentz, F. J., L. Ricciardulli, K. A. Hilburn and C. A. Mears, (2007) How much more rain will global warming bring?, *Science, 317*, 233-235.

Xie, X., W. T. Liu and B. Tang, (2008) Spacebased estimation of moisture transport in marine atmosphere using support vector regression, *Remote Sensing of Environment, 112*, 1846-1855.

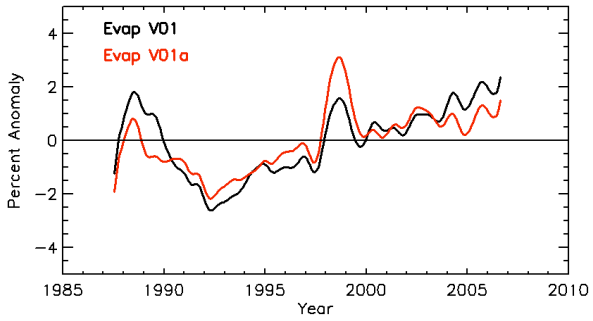

Figure 1. PMWC time series of evaporation without the wind correction (Version-1, black line) and with the wind correction (Version-1a, red line). Both time series have the same trend (1.26%/decade), however the Version-1a series has larger El Nino anomalies in 1998.

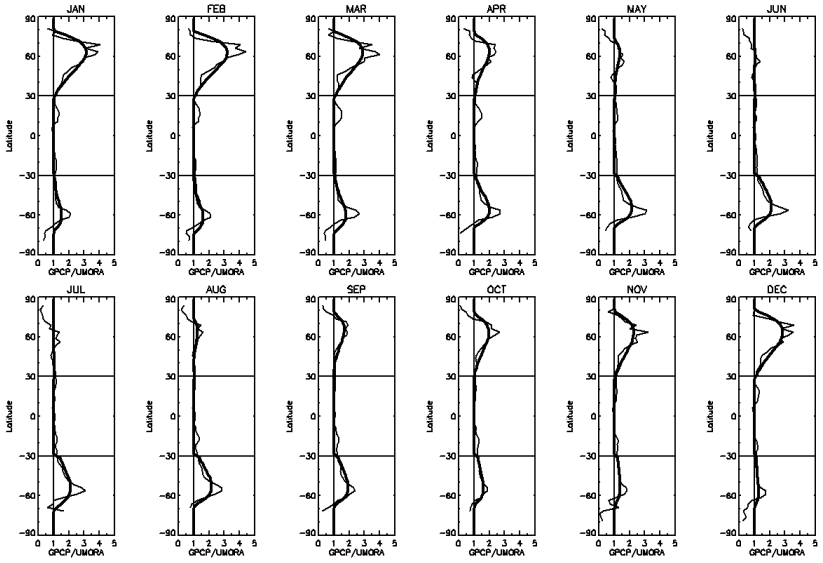

Figure 2. Multiplicative snow adjustment for each month based on the ratio of GPCP to REMSS rain rates. The thin curve is the raw ratio and the thick curve is the smoothed adjustment. Data from 1988-2005 are used.

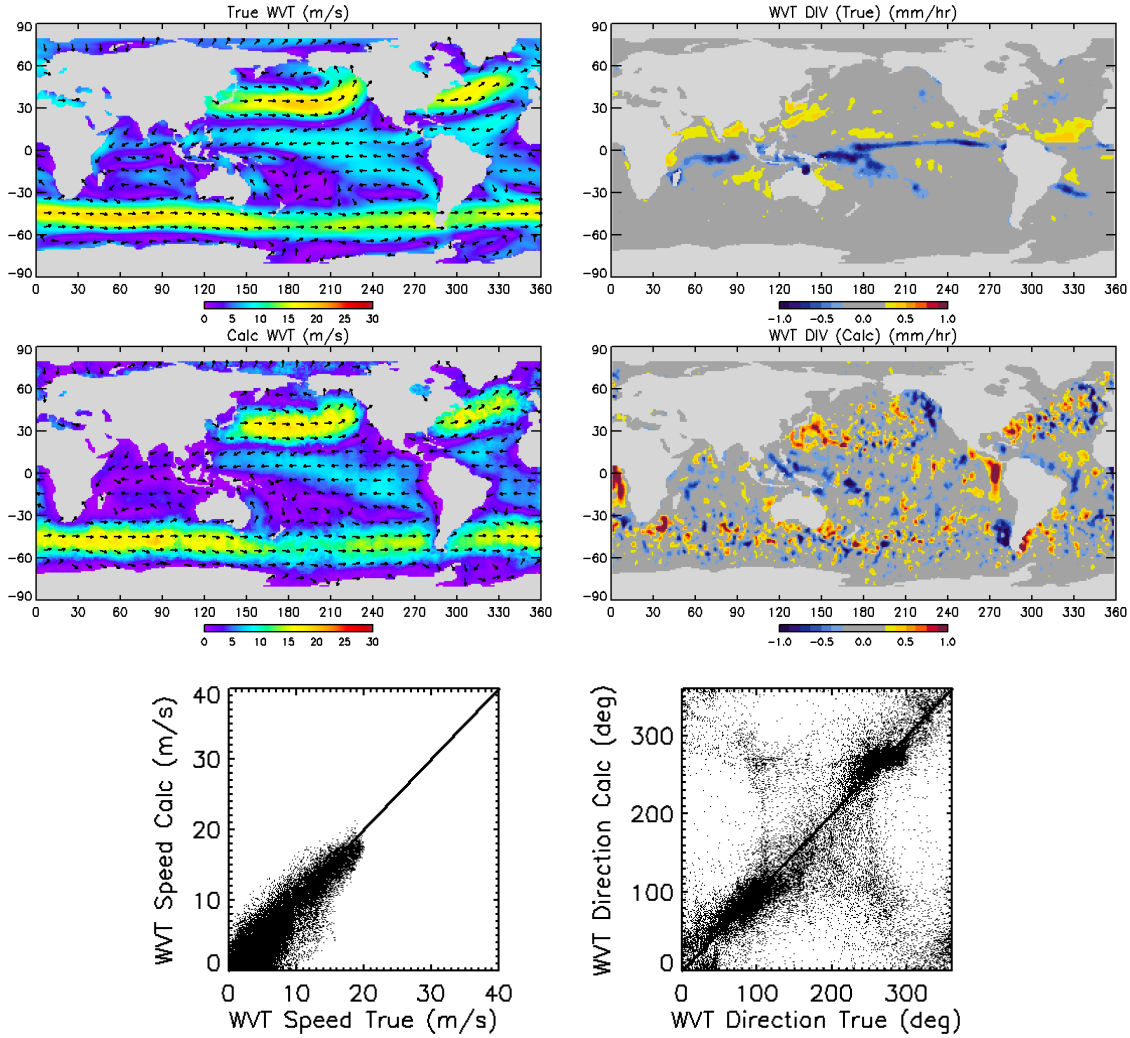

Figure 3. This is an example of results from feature tracking for January 2003. Shown are maps of water vapor transport: "true" (top, left) and calculated using feature tracking (middle, left); maps of water vapor transport divergence: "true" (top, right) and calculated from feature tracking transports (middle, right). At the bottom are scatterplots of transport speed (bottom, left) and direction (bottom, right).

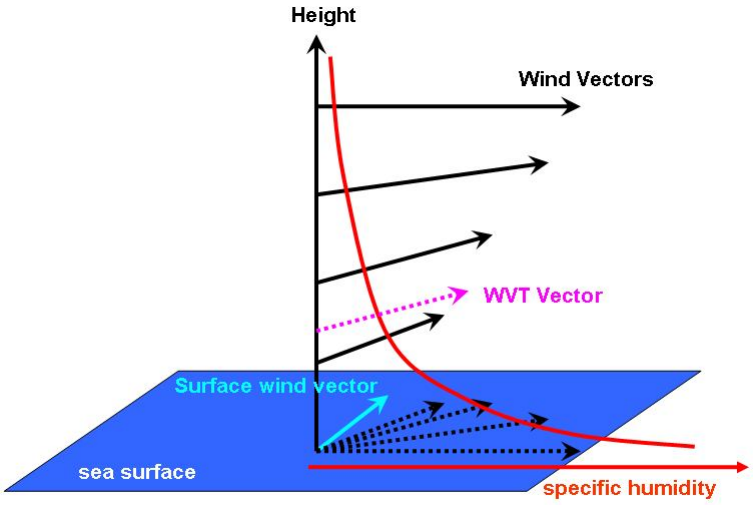

Figure 4. Schematic of the water vapor transport adjustment. This is the typical northern hemisphere example where anticyclonic turning with height means clockwise rotation with height.

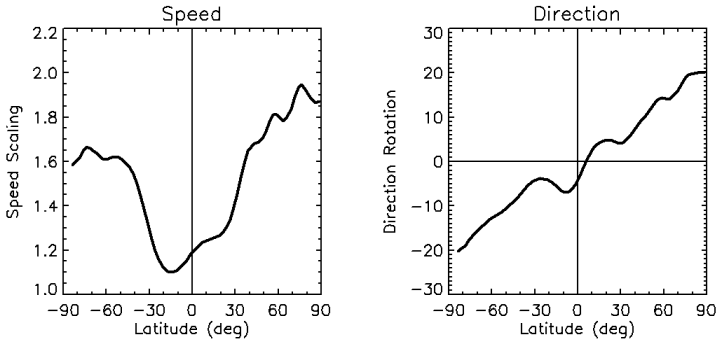

Figure 5. The surface to transport adjustment derived from NCEP as a function of latitude. Averages are for 2003.

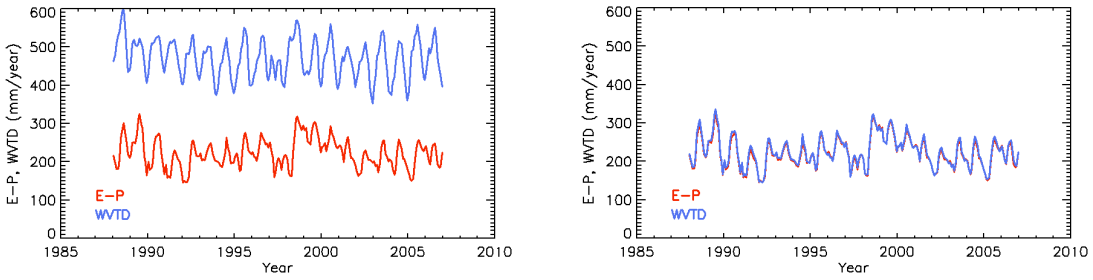

Figure 6. Time series of water vapor transport divergence (blue) and *E-P* (red) without divergence adjustment (left) and with the divergence adjustment (right).

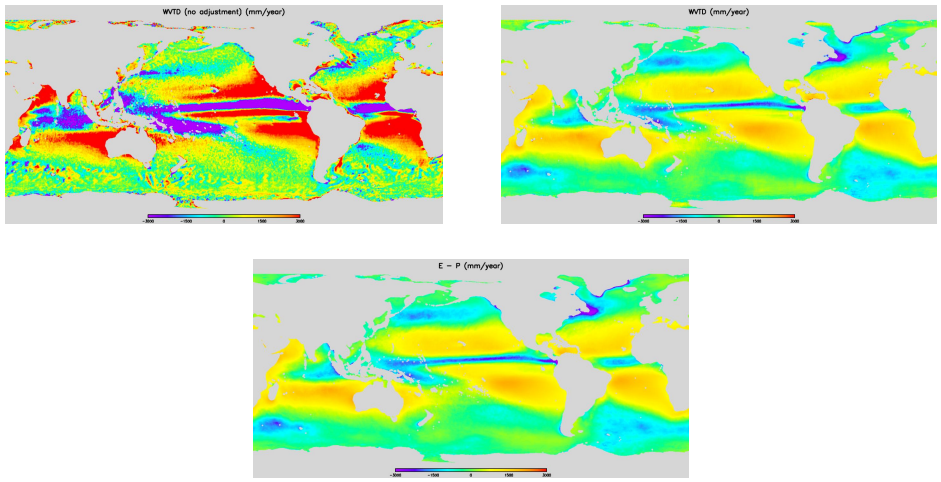

Figure 7. Maps of water vapor transport without the divergence adjustment (top, left), with the divergence adjustment (top, right) and *E-P* (bottom). The color scale goes from -3000 to 3000 mm/year. The time period for Figures 7, 8, and 9 is 1988-2006.

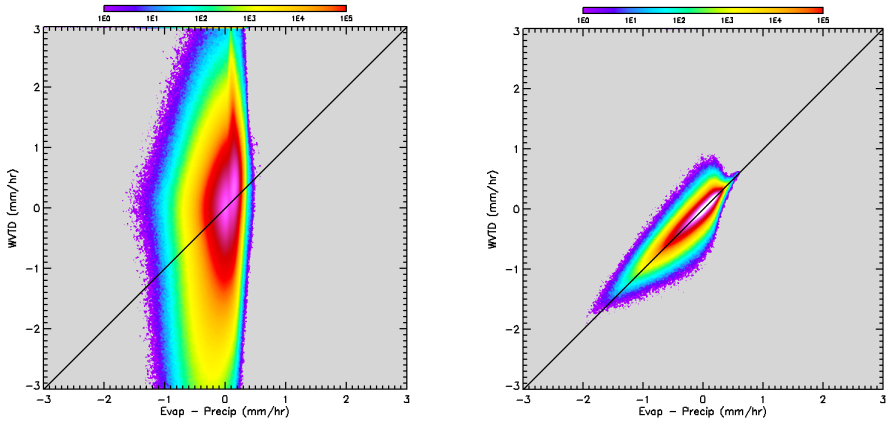

Figure 8. Joint histograms of water vapor transport divergence versus *E-P* without the divergence adjustment (left) and with the divergence adjustment (right). The logarithmic color scale indicates the number of observations. Observations poleward of 60° are excluded to avoid noisy pixels near the ice edge.

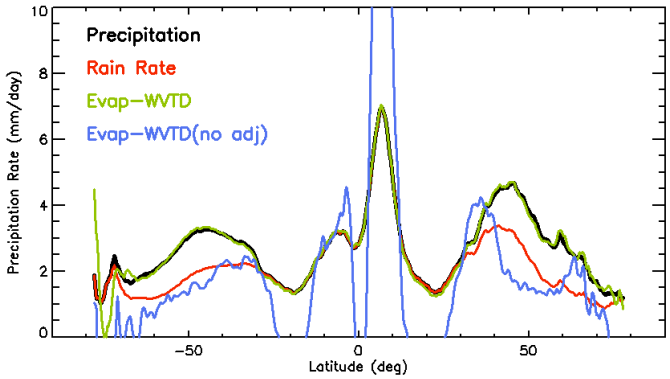

Figure 9. Zonal averages of precipitation (black), rain rate (red), and evaporation minus water vapor transport divergence without the divergence adjustment (blue) and with the divergence adjustment (green).

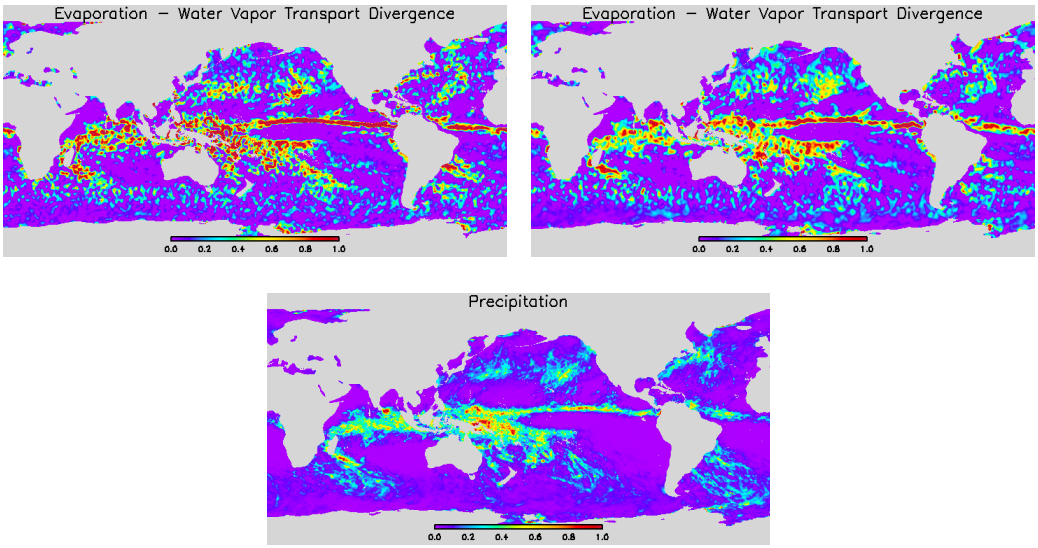

Figure 10. Precipitation implied by hydrological balance for January 2005: no wind data in raining areas (top, left), Atlas Level 3 data to fill in raining area data voids (top, right), and precipitation (bottom). The color scales go from 0 to 1 mm/hour.

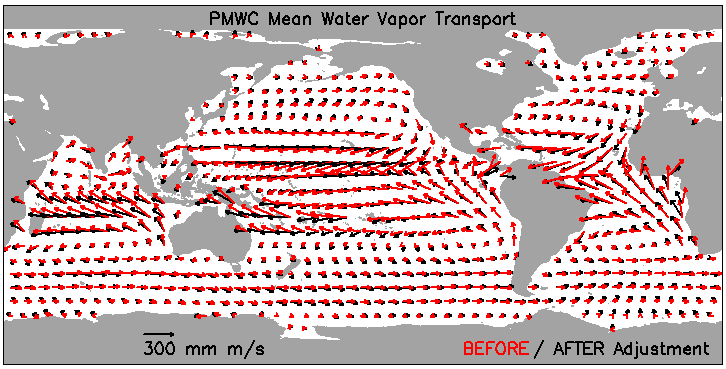

Figure 11. This example shows the change in vectors due to the divergence adjustment. This is the water vapor transport averaged for 1988-2006.

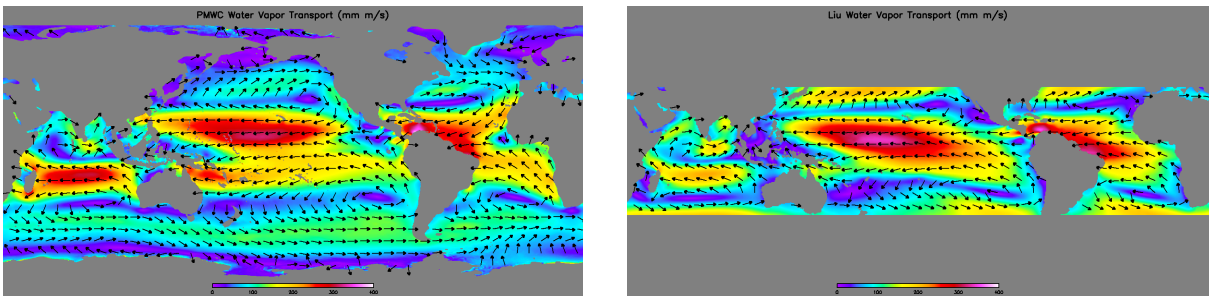

Figure 12. PMWC (left) and Liu (right) water vapor transport maps. The color scale reaches a maximum at 600 mm m/s. Figures 12, 13, 14, and 15 use the time period 2000-2005.

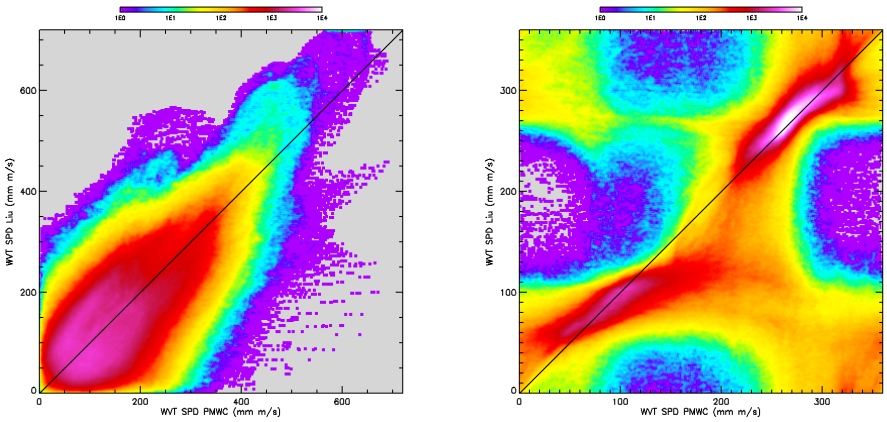

Figure 13. Joint PDFs of water vapor transport speed (left) and direction (right). PMWC is on the horizontal axis and Liu is on the vertical axis. The logarithmic color scale indicates the number of observations.

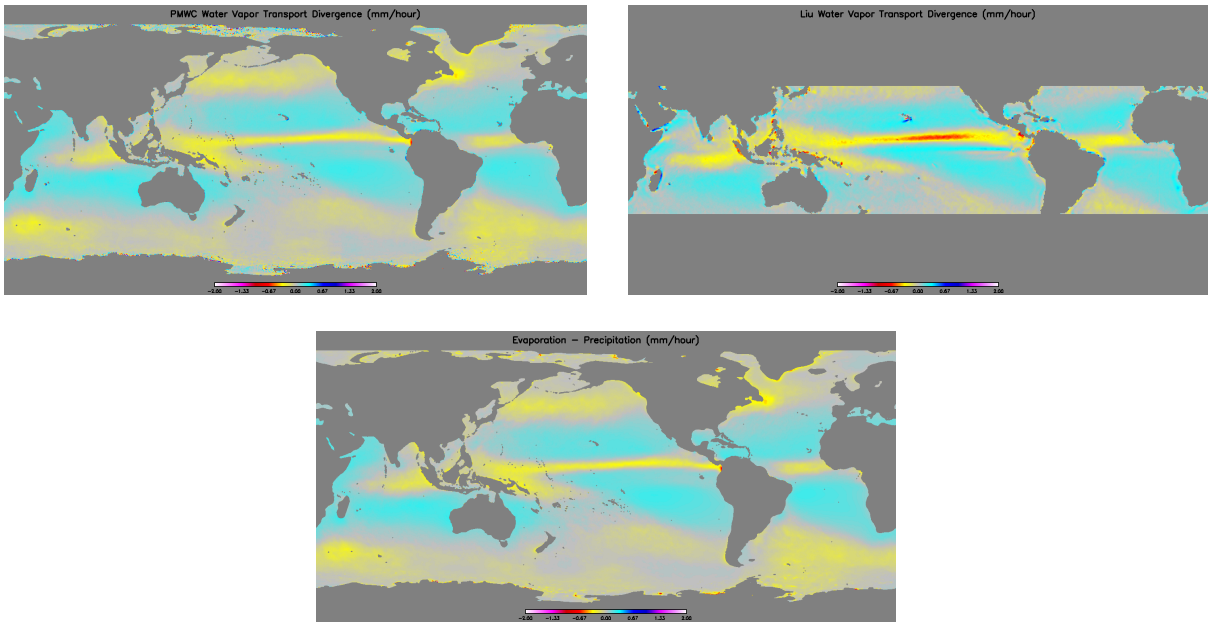

Figure 14. Shown are transport divergence maps for PMWC (top, left) and Liu (top, right) with *E-P* (bottom) shown for reference. The color scale goes from -2 to 2 mm/hour.

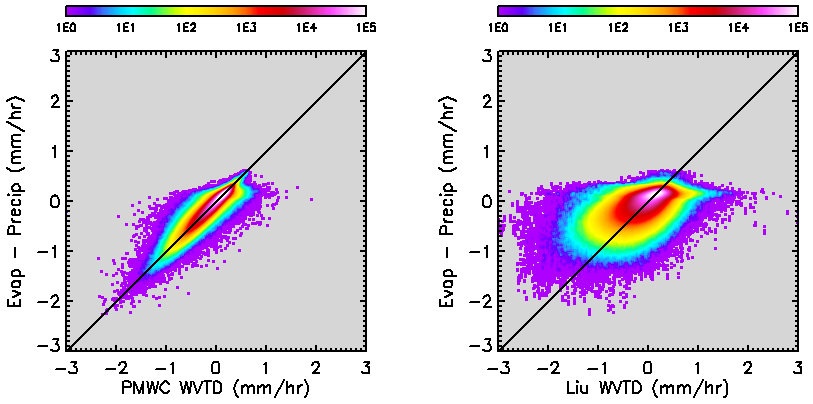

Figure 15. Joint PDFs of PMWC (left) and Liu (right) transport divergence on the horizontal axis versus *E-P* on the vertical axis. The logarithmic color scale indicates the number of observations.

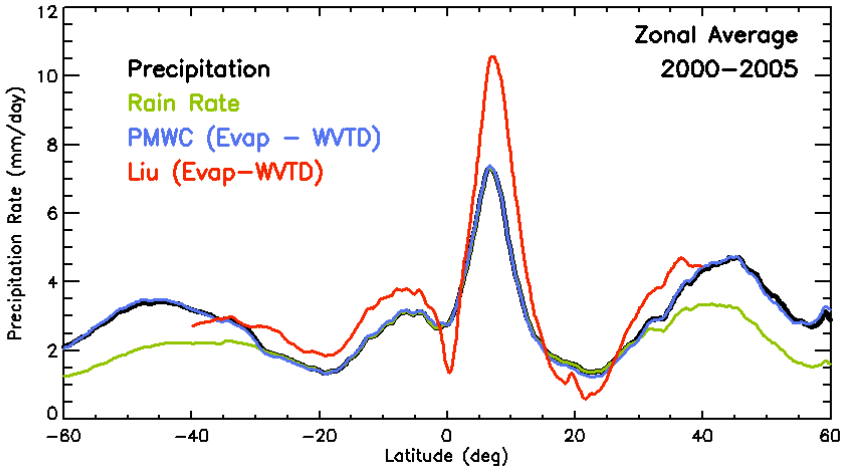

Figure 16. Zonal average precipitation implied by hydrological balance for PMWC (blue) and Liu (red) with precipitation (black) and rain rate (green) shown for reference.